Challenges of diagnosing glaucoma in myopic eyes

Qiu, Kunliang

Chapter 3

Retinal nerve fiber bundle trajectories in Chinese myopic eyes: comparison with a Caucasian based mathematical model

Kunliang Qiu, Mingzhi Zhang, Zhenggen Wu, Jukka Nevalainen, Ulrich Schiefer, You Huang, Nomdo M. Jansonius

Submitted

ABSTRACT

Purpose: To determine the characteristics of the retinal nerve fiber bundle (RNFB) trajectories in Chinese myopic eyes.

Methods: We collected high quality red free fundus images from 80 eyes of 80 Chinese myopic subjects (median [inter-quartile range] refraction -3.9 [-6.0 to -2.5] D). We traced all visible RNFBs and evaluated the characteristics of the RNFB trajectories using a previously published mathematical model based on Caucasian eyes. The influence of axial length, retinal vessel course, and optic disc anatomy on the trajectories was determined with multiple linear regression analysis.

Results: In the superior-temporal region, the RNFB trajectories of the Chinese myopic eyes were very similar to that of the Caucasian eyes. In the inferior-temporal region, the trajectories of the Chinese low to moderate myopic eyes were approximately similar to that of the Caucasian eyes; trajectories of the Chinese high myopic eyes were clearly less curved. In the superior-temporal region, the trajectories were associated with retinal vessel course ($P=0.008$) and optic disc size ($P=0.016$). In the inferior-temporal region, there was a significant association with axial length ($P<0.001$), retinal vessel course ($P=0.006$), and disc torsion ($P=0.009$).

Conclusions: The previous Caucasian based RNFB trajectory model can be applied to Chinese myopic subjects without modification; depending on the accuracy needed, a separate model for the inferior hemiretina could be considered in case of high myopia. Further research is needed to value personalisation based on retinal vessel topography and optic disc properties.

1. Introduction

Glaucoma is a chronic and progressive eye disease characterized by cupping of the optic disc, thinning of the retinal nerve fiber layer (RNFL), loss of retinal ganglion cells (RGCs), and loss of visual function. Integration of structural (for example, from the assessment of the optic disc) and functional (for example, from perimetry) information is pivotal for understanding the glaucomatous process; it requires a detailed anatomical knowledge of the retinal nerve fiber bundle (RNFB) trajectories. Previously, several models describing the RNFB trajectories have been reported (Garway-Heath et al., 2000; Wigelius, 2001; Ferreras et al., 2008; Turpin et al., 2009; Jansonius et al., 2009; Carreras et al., 2014). All these models were based on Caucasian eyes. Nowadays, Caucasians form only about one fifth of the world population; 60% of the world population lives in Asia. Also, the previous models did not specifically address myopia, whereas the prevalence of myopia - a major glaucoma risk factor (Marcus et al., 2011) - increases rapidly (Kempen et al., 2004; Liang et al., 2009; Morgan et al., 2012).

Myopia has been reported to be associated with tilted disc, increased intraocular pressure, and visual field defects. These factors challenge the diagnosis of glaucoma in myopic subjects. With the use of optical coherence tomography (OCT), it has been shown that myopic eyes have different profiles of the peripapillary RNFL compared to non-myopic (Hong et al., 2010; Leung et al., 2012). Besides, ethnic differences in RNFL thickness have been reported (Samarawickrama et al., 2010; Knight et al., 2012; Alasil et al., 2013; Rao et al., 2015). Previously, we developed a mathematical model describing the RNFB trajectories in Caucasian eyes and found that refraction was an important factor associated with the intersubject variability of the RNFB trajectories (Jansonius et al., 2009, 2012), which has been confirmed in other studies (Denniss et al., 2012; Lamparter et al., 2013). Optic disc position, shape, and size, and retinal blood vessel topography contributed to the inter-subject variability as well (Jansonius et al., 2012; Lamparter et al., 2013; Qiu et al., 2015). All this makes that it is important to validate the existing model in other ethnicities and myopic eyes.

The aim of this study was to determine the characteristics of the RNFB trajectories in Chinese myopic eyes. For this purpose, we collected high quality red free fundus images from a large group of healthy Chinese myopic subjects. We evaluated the characteristics of the RNFB trajectories using the previously published mathematical model based on Caucasian eyes, and we additionally determined the influence of axial length, retinal vessel course, and optic disc position, size, shape, and torsion on the trajectories.

2. Methods

2.1. Subjects

Myopic subjects were consecutively recruited from the general and refractive surgery clinic of the Joint Shantou International Eye Center. All the included subjects received a complete ophthalmic examination including the measurement of visual acuity, cycloplegic refraction using an autorefractor (Canon FK-1; Canon, Tokyo, Japan), axial length (IOL Master; Carl-Zeiss Meditec, Dublin, CA), and intraocular pressure (IOP), perimetry (see next section), and a stereoscopic fundus examination and photography with dilated pupils. The included eyes did not have any concurrent eye disease, other than a refractive error; we included eyes with a spherical equivalent less than -0.5 diopters (D); we did not set constrains regarding astigmatism. Based on the refractive status, the subjects were subdivided into two groups: low to moderate myopia (spherical equivalent between −0.50 and −6.00 D) and high myopia (spherical equivalent beyond -6.00 D). Subjects were excluded if the IOP was over 21 mmHg, the best corrected visual acuity less than 20/40, if they had a family history of glaucoma, or if they had a history of myopic macular degeneration, diabetes mellitus, neurological disease, refractive surgery, intraocular surgery, or glaucoma. We included one eye per subject; if both eyes were eligible, one eye was randomly chosen. The current study followed the tenets of the declaration of Helsinki and

was approved by the ethical committee of Joint Shantou International Eye Center. Written informed consent was obtained from all subjects before participation.

2.2. Visual field testing

Visual field tests were performed with standard automated perimetry (Humphrey Field Analyzer II; Carl Zeiss Meditec, Inc.) using the 24-2 grid and the SITA standard strategy. Only reliable visual field tests (with false positive and negative responses less than 10%, and fixation loss less than 20%) were included (Bengtsson et al., 2000; Junoy Montolio et al., 2012). All the included subjects had a visual field test that was within normal limits in the glaucoma hemifield test (GHT) and had a pattern standard deviation (PSD) with $P>0.05$.

2.3. Fundus photography and RNFB assessment

Red-free fundus photographs were taken with dilated pupils using a fundus camera (Visucam 200; Carl Zeiss Meditec AG, Jena, Germany) with a build-in blue filter of 495 nm wavelength at an angle of 45° with the fovea in the center. The resolution of the digital images was 2124 by 2056 pixels. Only pictures with a good image quality (at least four traceable trajectories) were selected for further analysis. In order to enhance the visibility of the RNFL bundles, brightness, contrast, and sharpness of the selected photographs were optimized using Adobe Photoshop (CS4; Adobe Systems, Mountain View, CA). Photographs of left eyes were mirrored along the vertical axis to match tracings from right eyes. Enhanced images were then uploaded into CorelDraw (12.0, Corel Inc., Ottawa, Canada), where the positions of the optic disc and fovea were marked manually by drawing a reference ellipse/circle that was aligned to the margin of the optic disc border and fovea, respectively. All visible RNFBs were then manually traced back to the optic disc (Fig. 1) as far as visible, by one of the authors (K.Q.). The coordinates of the traced trajectories were extracted and fitted with previously developed software (Jansonius et al., 2009).

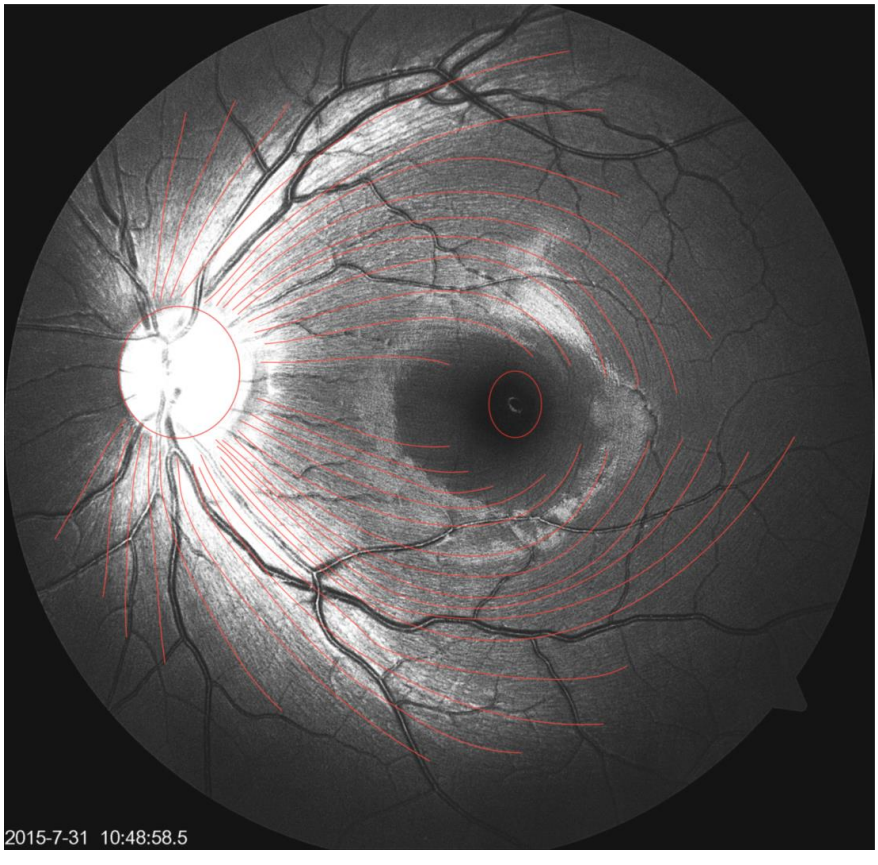

Figure 1. Example of a fundus photograph with traced trajectories.

2.4. Fitting RNFBs

The fitting process of the mathematical model has been described previously (Jansonius et al., 2009, 2012). In brief, the trajectories of the fibers were fitted in a modified polar coordinate system (r,φ), with its center located in the center of the optic disc, which was located at an eccentricity of (15°,2°) in Cartesian coordinates with the fovea at (0º,0º). Here, r represents the distance from the disc center and φ the corresponding angle. We assumed that a RNFB trajectory can be described in the above mentioned polar coordinate system (r,φ) by:

$$\phi(\phi_0, r) = \phi_0 + b(\phi_0)(r - r_0)^{c(\phi_0)} \quad (1)$$

where $\varphi_0 = \varphi(r = r_0)$ is the angular position of the trajectory at its starting point at a circle with radius r_0 around the center of the optic disc and b and c parameters. Radius r_0 was set to 4o. Parameter b represents the amount of curvature and c determines the location of the curvature (maximum curvature close to the disc for $c < 1$ and further away from the disc for $c > 1$). Parameter c, which is not critical (Jansonius et al., 2012), was set to its original value.

2.5. Blood vessel topography

The retinal blood vessel topography was mathematically described using the positions of the major temporal retinal blood vessels. Measurements were performed with ImageJ software (available in the public domain at http://rsbweb.nih.gov/ij/; www.nih.gov, National Institutes of Health, Bethesda, MD, USA). Firstly, the height and width of the optic disc was fitted by a rectangle. The crossing of the two diagonal lines of the rectangle was considered the optic disc center. Two circles with radii equaling 50% (circle a), and 100% (circle b) of the distance between the optic disc center and the fovea were then drawn around the optic disc center. The intersections of the major temporal retinal blood vessels (superior artery, superior vein, inferior artery, and inferior vein) and the circles were determined. The retinal vessel angles were defined as the angles subtended by a line connecting the optic disc center and the fovea and the lines connecting the optic disc center and the intersections. Subsequently, two series of four angles were defined: superior artery angle (SAAa and SAAb), superior vein angle (SVAa and SVAb), inferior artery angle (IAAa and IAAb), and inferior vein angle (IVAa and IVAb). Figure 2 shows the two circles and the angles at circle a.

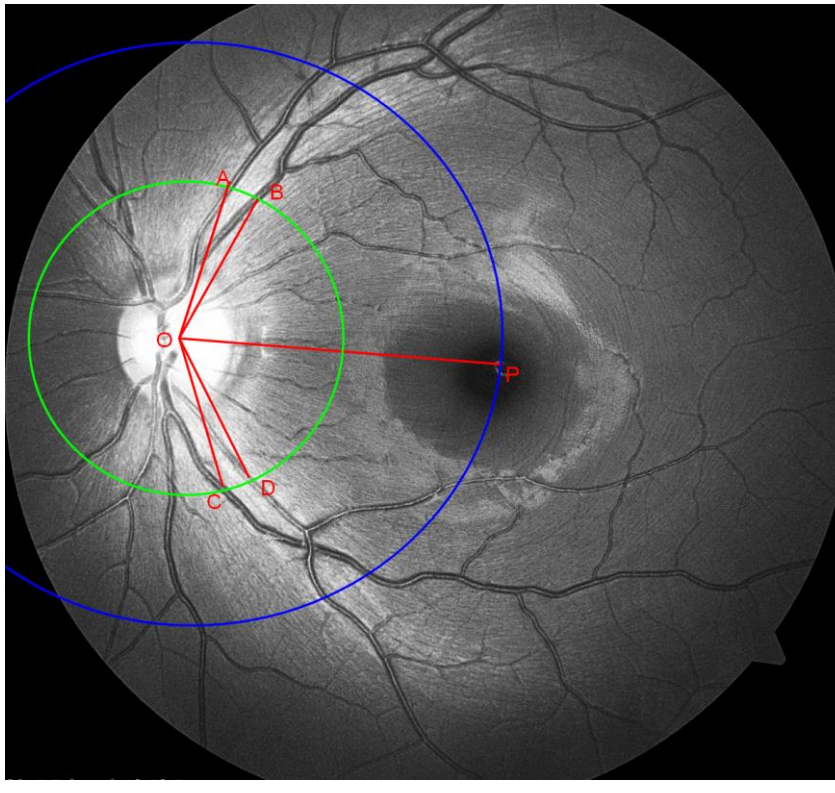

Figure 2. Blood vessel angles were defined at different distances from the optic nerve head (optic disc) using the intersections of the major temporal retinal blood vessels (superior artery, superior vein, inferior artery, and inferior vein) and two circles around the optic disc center. These angles were defined for circles with radii of 50% (circle 1; green), 100% (circle 2; blue). Angles at circle: superior arterial angle (SAA; A-P), superior venous angle (SVA; B-P), inferior arterial angle (IAA; D-P), and inferior venous angle (IVA; C-P).Vertex at O for all angles.

2.6. Optic disc inclination, size, shape, and torsion

Measurements of optic disc inclination, size, shape, and torsion were performed with ImageJ software on the fundus images. Inclination of the optic disc was defined as the angle (in degrees) between a line connecting the optic disc center and the fovea and a horizontal line through the fovea. The margin of the optic disc was defined by the inner border of the scleral rim and fitted with an ellipse. Optic disc size was subsequently determined with a magnification correction according to the method of Bennett et al (Bennett et al., 1994). Optic disc shape was measured as the ovality index (defined as the shorter diameter divided by the longer diameter; Tay et al., 2005). Disc torsion was defined as the deviation (in

degrees) of the longer axis of the optic disc from a line perpendicular to the line connecting the fovea and the disc center. A positive torsion value indicates a counterclockwise torsion in the right eye format, a negative value a clockwise torsion.

2.7. Data analysis

The superior-temporal and inferior-temporal region were analyzed separately. The fitting process yielded an ln b (superior half of the retina) or ln(-b) (inferior half) value for each RNFB trajectory. The b values of the newly traced trajectories from the current study population were compared to the previously found relationship between φ_0 and b in Caucasian eyes (Jansonius et al., 2009). In the superior-temporal region, this relationship can be described by:

$$\ln b = -1.9 + 3.9 \tanh(-(\phi_0 - 121)/14) \quad (2)$$

with -1.9 replaced by -2.5 or -1.3 to describe the 95% central range. In the inferior-temporal region, the relationship can be described by:

$$\ln(-b) = 0.7 + 1.5 \tanh(-(-\phi_0 - 90)/25) \quad (3)$$

with 0.7 replaced by 0.1 or 1.3 to describe the 95% central range. The percentage of the newly traced trajectories that had a (φ_0,b) combination within the 95% central range of the existing model was subsequently determined for both regions.

Correlation analysis and multiple linear regression analysis were performed to uncover factors associated with subject specific deviations from the model. For this purpose, we calculated, for each subject, a mean departure, for the superior-temporal and inferior-temporal region separately. The deviation of a trajectory from the model was calculated as the difference between the ln b or ln(-b) value of the trajectory and the corresponding predicted ln b or ln(-b) value of the model. Subsequently, the mean departure was calculated as the average difference within the superior-temporal ($60 \leq \varphi_0 \leq 180^o$) and inferior-temporal region ($165 < \varphi_0 \leq 60^o$; inferior papillomacular bundle excluded from this analysis; see Discussion

section). All the statistical analyses were performed with SPSS (ver. 23.0; SPSS Inc, Chicago, IL). A P value of 0.05 or less was considered statistically significant.

3. Results

A total of 80 eyes from 80 myopia subjects (41 males, 39 females) were included in this prospective study. Table 1 shows the demographic data of the study population. The median spherical equivalent of the included eyes was 3.9 D (range 10.0 to 1.0 D); median cylinder power was 0.50 D (range 1.5 to 0 D). Sixty eyes had low to moderate myopia; 20 eyes had high myopia. Spherical equivalent was significantly associated with axial length ($r = 0.79$; $P<0.001$); the optic disc parameters were only weakly correlated with each other (correlation coefficients between 0.04 and +0.19). Similar weak correlations were found between the optic disc parameters and axial length, the optic disc parameters and the vessel angles, the vessel angles and the axial length, and the arterial angles and corresponding vein angles (correlation coefficients between 0.35 and +0.40).

Table 1. Characteristics of the included eyes (n=80)

	Median	IQR	Range
Age, y	24.1	20.0 to 28.8	18 to 44
Refraction, D	-3.9	-6.0 to -2.5	-10.0 to -1.0
Axial length, mm	25.1	24.6 to 25.8	22.0 to 28.1
Optic disc size, mm2	1.84	1.64 to 2.06	1.18 to 2.60
optic disc inclination, deg	7.0	4.3 to 9.5	-1.8 to 16.9
Optic disc shape	0.81	0.76 to 0.87	0.67 to 0.95
Optic disc torsion, deg	-7.4	-15.9 to 3.8	-40.9 to 39.5
SAAa, deg	61.0	55.7 to 65.6	42.5 to 82.0
SVAa, deg	57.8	50.8 to 70.2	34.2 to 93.7
IAAa, deg	61.9	55.0 to 70.5	29.1 to 87.2
IVAa, deg	65.9	57.9 to 75.8	45.6 to 121.1
SAAb, deg	47.8	43.9 to 54.0	21.6 to 71.0
SVAb, deg	45.0	37.0 to 52.6	26.1 to 72.0
IAAb, deg	52.0	44.1 to 58.9	21.9 to 73.0
IVAb, deg	55.4	47.3 to 63.2	33.3 to 82.0
Mean departure superior-temporal	-0.06	-0.27 to 0.12	-0.83 to 0.79
Mean departure inferior-temporal	-0.22	-0.38 to 0.12	-1.31 to 0.33

IQR = inter-quartile range; SAAa,b = superior artery angle at circle a,b; SVAa,b = superior vein angle at circle a,b; IAAa,b = inferior artery angle at circle a,b; IVAa,b = inferior vein angle at circle a,b.

In total, 1460 RNFBs, based on 21,658 sampling points, were manually traced. On average (mean ± standard deviation [SD]), 18.4 ± 6.4 (range 4 to 37) bundles were traced per subject with a mean of 14.8 ± 5.4 (4 to 38) sampling points per RNFB. The number of traced trajectories per subject was not correlated with the spherical equivalent (r = 0.04; P=0.72). Figure 3 shows parameter b as a function of φ_0, presented as ln b for the superior-temporal region (A) and ln(-b) for the inferior-temporal region (B). The two lines represent the 95% central range from the earlier published model. In the superior-temporal region, 564 of 656 trajectories (86%) were within the 95% central range of the model. This was 563 of 683 (82%) for the inferior-temporal region. After excluding trajectories with

$\varphi_0 \leq 165^o$ (due to significant deviation of the inferior papillomacular bundle from the model; see Discussion section), 561 of 660 trajectories (85%) were within the 95% central range of the model in the inferior-temporal region. For the superior-temporal region, subgroup analysis revealed that 444 of 511 (87%) and 120 of 145 (83%) trajectories were within the 95% central range of the model in the mild to moderate and high myopic eyes, respectively (P=0.22). For the inferior-temporal region, this was 437 of 514 (85%) and 126 of 169 (75%), respectively (P=0.002). The median (inter-quartile range [IQR]) difference between ln b and the model for the 656 trajectories in the superior-temporal region was -0.01 (-0.32 to 0.26); this was 0.00 (-0.30 to 0.26) for low/moderate myopia and -0.03 (-0.40 to 0.23) for high myopia. The median (IQR) difference between ln(-b) and the model for the 660 trajectories in the inferior-temporal region was -0.13 (-0.39 to 0.09); this was -0.07 (-0.34 to 0.13) for low/moderate myopia and -0.28 (-0.55 to -0.06) for high myopia. Hence, the trajectories of the Chinese myopic eyes fit in the Caucasian trajectory model generally quite well, except for high myopia in the inferior-temporal region. Figure 4 shows the original model (black trajectories) as described by Eqs. (2) and (3), and a separate model for the inferior-temporal region for the high myopic Chinese eyes (magenta trajectories; Fig. 4B; for this model we replaced in Eq. (3) 0.7 by 0.70.28=0.42). For high myopia, the Chinese trajectories were less curved than that of the Caucasian model.

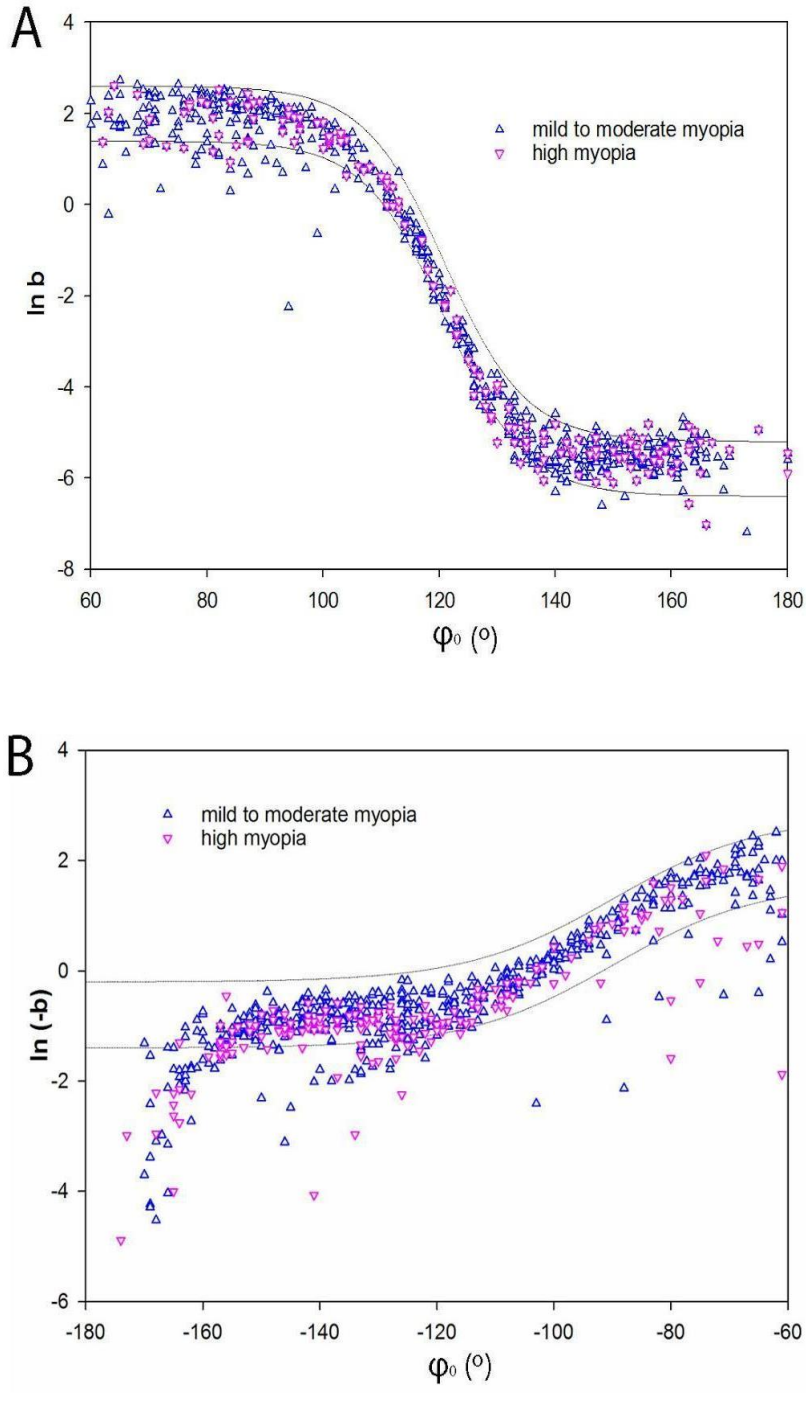

Figure 3. Parameter b as a function of φ_0, presented as ln b for the superior-temporal region (A) and ln(-b) for the inferior-temporal region (B). The two lines represent the 95% central ranges from the earlier published model based on Caucasian eyes (Jansonius et al., 2009). Data points from both the mild to moderate myopia (blue triangle up) and the high myopia (magenta triangle down).

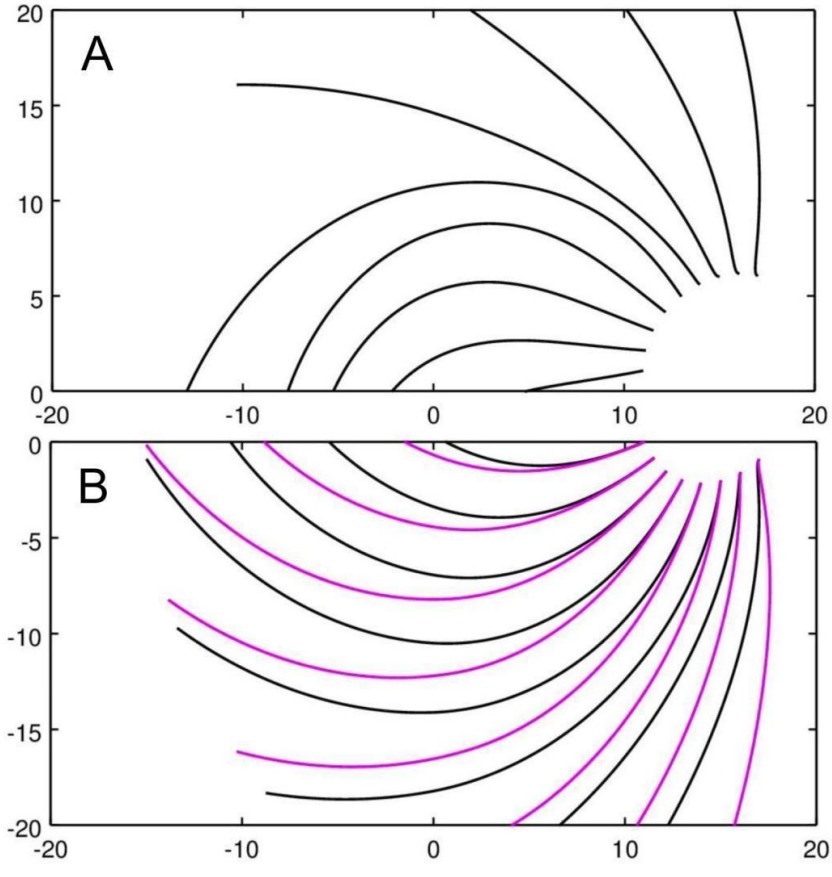

Figure 4. Trajectory model for the superior-temporal region (A) and inferior-temporal region (B). A: original model (black) coincides with Chinese model for all myopia. B: original model (black) and Chinese model for high myopia (magenta). Trajectories shown for φ_0 from 60 to 180^o (A) and from -165 to -60^o (B) with a resolution of 15^o. Numbers along the axes refer to retinal position in degrees, in Cartesian coordinates.

In the superior-temporal region, there was a significant association between mean departure and SAAa, SAAb, optic disc size, and optic disc torsion; in the inferior-temporal region, there was a significant association between mean departure and axial length, IAAa, IAAb, and disc torsion (Table 2). Table 3 shows the corresponding multiple regression analysis. We a priori left out spherical equivalent because of its high correlation with axial length. Similarly, we built separate models for SAAa and SAAb, and for IAAa and IAAb. In the superior-temporal region, artery angle (SAAa or SAAb) and optic disc size were the only factors associated with the mean departure after adjusting for the other covariates.

In the inferior-temporal region, axial length, artery angle (IAAa or IAAb), and disc torsion were independently associated with mean departure.

Table 2. Correlation analysis between mean departure (average individual deviation from the model) and axial length, optic disc inclination, shape, size, and torsion, and blood vessel angles

	Mean departure superior-temporal		Mean departure inferior-temporal	
	r	P value	r	P value
Axial length	0.03	0.78	-0.36	0.002
Optic disc size	0.27	0.022	0.14	0.26
optic disc inclination	-0.06	0.61	0.13	0.25
Optic disc shape	0.08	0.48	0.06	0.59
Optic disc torsion	-0.24	0.036	-0.25	0.028
SAAa	0.29	0.010	/	/
SVAa	0.19	0.096	/	/
SAAb	0.31	0.005	/	/
SVAb	0.16	0.16	/	/
IAAa	/	/	0.39	<0.001
IVAa	/	/	0.18	0.12
IAAb	/	/	0.31	0.005
IVAb	/	/	0.10	0.37

SAAa,b = superior artery angle at circle a,b; SVAa,b = superior vein angle at circle a,b; IAAa,b = inferior artery angle at circle a,b; IVAa,b = inferior vein angle at circle a,b.

Table 3. Factors associated with the mean departure (average individual deviation from the model) in the superior-temporal (A,B) and the inferior-temporal region (C,D)

		R^2	Coefficient	Standard error	P value
A. superior-temporal		**0.12**			
	Intercept		-0.890	0.294	0.003
	SAAa		0.008	0.004	0.072
	Disc size		0.202	0.112	0.041
B. superior-temporal		**0.16**			
	Intercept		-0.982	0.257	<0.001
	SAAb		0.011	0.004	0.008
	Disc size		0.203	0.115	0.016
C. inferior-temporal		**0.31**			
	Intercept		2.006	0.718	0.007
	Axial length		-0.106	0.027	<0.001
	IAAa		0.006	0.002	0.006
	Disc torsion		-0.005	0.002	0.009
D. inferior-temporal		**0.28**			
	Intercept		2.238	0.723	0.003
	Axial length		-0.109	0.028	<0.001
	IAAb		0.005	0.002	0.035
	Disc torsion		-0.004	0.002	0.013

SAAa, b = superior artery angle at circle a, b; IAAa, b = inferior artery angle at circle a, b.

4. Discussion

The RNFB trajectories of Chinese eyes with low or moderate myopia are similar to that of Caucasians eyes that were not selected regarding refraction. For high myopia, the trajectories in the superior hemifield are similar to that of the Caucasians; in the inferior hemifield they follow a different pattern. Axial length, vessel topography, and optic disc size and torsion are associated with the trajectories but explain only a small part of the variability.

4.1. Factors that influence the RNFL trajectories

Factors that influence the RNFB trajectories have been studied using between-subject variability in various RNFB trajectory models and - more indirectly - by analyzing the peripapillary RNFL thickness distribution. Refraction/axial length was identified as an RNFB trajectory influencing factor previously, in Caucasian eyes (Jansonius et al., 2012; Denniss et al., 2012; Lamparter et al., 2013; Qiu et al., 2015), as was optic disc position (Denniss et al., 2012; Lamparter et al., 2013; Qiu et al., 2015), size (Denniss et al., 2012; Lamparter et al., 2013), and shape (Lamparter et al., 2013). Retinal blood vessel topography had a very strong influence as well (Qiu et al., 2015). In the current, Chinese myopic data, we confirmed the strong influence of the retinal blood vessel topography and the effect had the same direction and was of similar size. Axial length played a significant role in the Chinese myopic data as well, but only in the inferior hemiretina. This contrasts our analysis in the Caucasian eyes, where the influence was more pronounced in the superior hemiretina (Jansonius et al., 2012; Qiu et al., 2015). This might reflect an ethnicity difference, but the samples also differed in refraction distribution; the Caucasian sample was centered around emmetropia and contained only two subject beyond 6 D (mean [SD] spherical equivalent in the Caucasian sample 0.4 [3.3] D). Possibly, myopia only really influences the trajectories in case of high myopia (see below).

Studies that addressed the trajectories indirectly by assessing the peripapillary RNFL thickness distribution with OCT also showed an influence of myopia (Hong et al., 2010; Kim et al., 2010; Leung et al., 2012). Kim et al. reported that the temporal RNFL thickness was significantly thicker in moderate and high myopia compared to low myopia. Leung et al. measured the RNFL distribution angle (the angle between the radial axes of the superotemporal and inferotemporal RNFL bundles as determined in the RNFL thickness map) in 189 myopic eyes from 103 normal healthy myopic subjects. They demonstrated that the superotemporal and inferotemporal RNFL bundles converge temporally with increasing myopia. Hong et al. found that the angle between the peaks of the peripapillary RNFL profile decreased significantly with increasing myopia. A thicker temporal RNFL and a smaller RNFL distribution angle with increasing

myopia agrees with the direction of the effect of myopia we found. This can easily be seen in Fig. 4B: for a given position at the retina, the high myopia trajectories (magenta) run towards a more temporal location than the default trajectories (black). The same direction of the effect of refraction was found in the superior hemiretina in the Caucasian sample (Jansonius et al., 2012). The relationship between retinal vessel topography and the peripapillary RNFL thickness profile has been well described (Yamashita et al., 2013; Pereira et al., 2014). In line with these previous studies, we found that the retinal artery angle was significantly associated with the variability of the RNFB trajectories in both the superior-temporal and inferior-temporal region.

4.2. Limitations

This study has limitations. Although we spent much effort in improving the image quality as much as possible, the number of traceable trajectories per image was sometimes low (mean value 18; range 4 to 37). A comparison of our two earlier studies in Caucasians, which differed largely regarding the number of trajectories per image (3 to 118 with a mean of 30 trajectories per image versus 24 per image, evenly distributed over the clock hours, in all subjects), revealed that this is not a critical factor (Jansonius et al., 2009; Jansonius et al., 2012). Also, the tracing process is hampered by inter-observer variability (Denniss et al., 2014). We showed previously that the inter-observer variability of the tracing process was small compared to the variability between subjects (Jansonius et al., 2012). As the fundus images were taken at an angle of 45 degrees (that is, up to an eccentricity of 22.5 degrees), too little information was available from the nasal region and therefore we limited the current analysis to the superior-temporal and inferior-temporal region. However, this would not limit the use of the model in glaucoma too much since the nasal retina is rarely affected in early glaucoma and the model covers the majority and most relevant part of the area covered by modern 24-2 grid perimetry and OCT. As can be seen in Fig. 3B, the data points clearly deviate from the model in the inferior papillomacular bundle ($180 < \varphi 0 \leq 165^{o}$). This deviation was not found in the original model (as there were almost no

observations in this region; Jansonius et al., 2009) but, interestingly, it actually was observed in our replication study (Jansonius et al., 2012). The deviation corresponds to an overestimation by the model of the curvature of the trajectories in the inferior papillomacular bundle; in Fig. 4B this affects only the small region between the raphe and the first drawn trajectory. Strengths are the large sample size and the involvement of Asian myopes, which form the largest population on earth.

4.3. High myopia

Interestingly, in the inferior-temporal region, we found that significantly less RNFB trajectories of the high myopic eyes were within the 95% central range of the model than that of the mild to moderate myopic eyes (75% vs 85%, P=0.002), showing that the RNFB trajectories of high myopic eyes follow a different pattern (Figure 4B). Depending on the accuracy needed, this should be taken into account when applying the model, or not. For a given retinal location, the deviation at the level of optic disc insertion point is approximately 10 degrees. The reasons for this deviation, and why it is more pronounced inferiorly, remains to be uncovered. Presumably, it is related to the different globe shape in high myopia. Instead of a spherical globe, high myopic eyes demonstrate a symmetrical or asymmetrical anteroposterior elongation and posterior protrusion (Moriyama et al., 2011), and this may results in various shapes, including spheroidal, ellipsoidal, conical, nasally distorted, temporally distorted, and barrel shapes (Guo et al., 2017; Wen et al., 2017; Pope et al., 2017). During development, the elongation of the globe could be asymmetrical and this might explain why axial length and disc torsion affect the RNFB trajectories mainly in the inferior-temporal region. The superior visual field defects that are found in profound high myopia support the existence of such an asymmetry. These visual field defects disappear with appropriate refraction to compensate the asymmetrical shape of the globe (Riise et al., 1966).

4.4. Conclusions

We were able to validate our Caucasian based RNFB trajectory model in Chinese myopic subjects. The original model can be applied to this population without modification; depending on the accuracy needed, a separate model for the inferior hemiretina could be considered in case of high myopia. Further research is needed to value personalization based on retinal vessel topography and optic disc properties.

References

Alasil T, Wang K, Keane PA, et al. Analysis of normal retinal nerve fiber layer thickness by age, sex, and race using spectral domain optical coherence tomography. J Glaucoma. 2013;22:532-541.

Bengtsson B, Heijl A. False-negative responses in glaucoma perimetry: indicators of patient performance or test reliability?Invest Ophthalmol Vis Sci. 2000;41:2201-2204.

Bennett AG, Rudnicka AR, Edgar DF. Improvements on Littmann's method of determining the size of retinal features by fundus photography. Graefes Arch Clin Exp Ophthalmol. 1994;232:361-367.

Carreras FJ, Medina J, Ruiz-Lozano M, Carreras I, Castro JL. Virtual tissue engineering and optic pathways: plotting the course of the axons in the retinal nerve fiber layer. Invest Ophthalmol Vis Sci. 2014; 55:3107-3119.

Denniss J, McKendrick AM, Turpin A. An anatomically customizable computational model relating the visual field to the optic nerve head in individual eyes. Invest Ophthalmol. Vis. Sci. 2012;53:6981-6990.

Denniss J, Turpin A, Tanabe F, Matsumoto C, McKendrick AM. Structure-function mapping: variability and conviction in tracing retinal nerve fiber bundles and comparison to a computational model. Invest Ophthalmol Vis Sci. 2014;55:728-736.

Ferreras A, Pablo LE, Garway-Heath DF, Fogagnolo P, Garcia-Feijoo J. Mapping standard automated perimetry to the peripapillary retinal nerve fiber layer in glaucoma. Invest. Ophthalmol. Vis. Sci. 2008;49:3018-3025.

Garway-Heath DF, Poinoosawmy D, Fitzke FW, Hitchings RA. Mapping the visual field to the optic disc in normal tension glaucoma eyes. Ophthalmology 2000;107:1809-1815.

Guo X, Xiao O, Chen Y, et al. Three-Dimensional Eye Shape, Myopic Maculopathy, and Visual Acuity: The Zhongshan Ophthalmic Center-Brien Holden Vision Institute High Myopia Cohort Study. Ophthalmology. 2017;124:679-687.

Hong SW, Ahn MD, Kang SH, Im SK. Analysis of peripapillary retinal nerve fiber distribution in normal young adults. Invest Ophthalmol Vis Sci. 2010;51:3515-3523.

Jansonius NM, Nevalainen J, Selig B, et al. A mathematical description of nerve fiber bundle trajectories and their variability in the human retina. Vis. Res. 2009;49:2157-2163.

Jansonius NM, Schiefer J, Nevalainen J, Paetzold J, Schiefer U. A mathematical model for describing the retinal nerve fiber bundle trajectories in the human eye:

average course, variability, and influence of refraction, optic disc size and optic disc position. Exp Eye Res. 2012;105:70-78.

Junoy Montolio FG, Wesselink C, Gordijn M, Jansonius NM. Factors that influence standard automated perimetry test results in glaucoma: test reliability, technician experience, time of day, and season. Invest Ophthalmol Vis Sci. 2012;53:7010-7017.

Kempen JH, Mitchell P, Lee KE, et al. The prevalence of refractive errors among adults in the United States, Western Europe, and Australia. Arch Ophthalmol. 2004;122:495-505.

Kim MJ, Lee EJ, Kim TW. Peripapillary retinal nerve fibre layer thickness profile in subjects with myopia measured using the Stratus optical coherence tomography. Br J Ophthalmol. 2010;94:115-120.

Knight OJ, Girkin CA, Budenz DL, et al. Effect of race, age, and axial length on optic nerve head parameters and retinal nerve fiber layer thickness measured by Cirrus HD-OCT. Arch Ophthalmol. 2012;130:312-318.

Lamparter J, Russell RA, Zhu H, et al. The influence of intersubject variability in ocular anatomical variables on the mapping of retinal locations to the retinal nerve fiber layer and optic nerve head.Invest Ophthalmol Vis Sci. 2013;54:6074-6082.

Leung CK, Yu M, Weinreb RN, et al. Retinal nerve fiber layer imaging with spectral-domain optical coherence tomography: interpreting the RNFL maps in healthy myopic eyes. Invest Ophthalmol Vis Sci. 2012;53:7194-7200.

Liang YB, Wong TY, Sun LP, et al. Refractive errors in a rural Chinese adult population the Handan eye study. Ophthalmology. 2009;116:2119-2127.

Marcus MW, de Vries MM, Junoy Montolio FG, Jansonius NM. Myopia as a risk factor for open-angle glaucoma: a systematic review and meta-analysis. Ophthalmology. 2011;118:1989-1994.

Morgan IG, Ohno-Matsui K, Saw SM. Myopia. Lancet. 2012;379:1739-1748.

Moriyama M, Ohno-Matsui K, Hayashi K, et al. Topographic analyses of shape of eyes with pathologic myopia by high-resolution three-dimensional magnetic resonance imaging. Ophthalmology. 2011;118:1626-1637.

Pereira I, Weber S, Holzer S, et al. Correlation between retinal vessel density profile and circumpapillary RNFL thickness measured with Fourier-domain optical coherence tomography. Br J Ophthalmol. 2014;98:538-543.

Pope JM, Verkicharla PK, Sepehrband F, Suheimat M, Schmid KL, Atchison DA. Three-dimensional MRI study of the relationship between eye dimensions, retinal shape and myopia. Biomed Opt Express. 2017;8:2386-2395.

Qiu K, Schiefer J, Nevalainen J, Schiefer U, Jansonius NM. Influence of the Retinal Blood Vessel Topography on the Variability of the Retinal Nerve Fiber

Bundle Trajectories in the Human Retina. Invest Ophthalmol Vis Sci. 2015;56:6320-6325.

Rao R, Dhrami-Gavazi E, Al-Aswad L, Ciarleglio A, Cioffi GA, Blumberg DM. Optic Nerve Head and Retinal Nerve Fiber Layer Differences Between Caribbean Black and African American Patients as Measured by Spectral Domain OCT. J Glaucoma. 2015;24:e43-46.

Riise D. Visual field defects in optic disc malformation with ectasia of the fundus. Acta ophthalmologica. 1966;44:906-918.

Samarawickrama C, Wang JJ, Huynh SC, et al. Ethnic differences in optic nerve head and retinal nerve fibre layer thickness parameters in children. Br J Ophthalmol. 2010;94:871-876.

Tay E, Seah SK, Chan SP, et al. Optic disk ovality as an index of tilt and its relationship to myopia and perimetry. Am J Ophthalmol. 2005;139:247-252.

Turpin A, Sampson GP, McKendrick AM. Combining ganglion cell topology and data of patients with glaucoma to determine a structure-function map. Invest. Ophthalmol. Vis. Sci. 2009;50:3249-3256.

Wen B, Yang G, Cheng J, et al. Using High-Resolution 3D Magnetic Resonance Imaging to Quantitatively Analyze the Shape of Eyeballs with High Myopia and Provide Assistance for Posterior Scleral Reinforcement. Ophthalmologica. 2017;238:154-162.

Wigelius O. A Model for the Retinal Nerve Fiber Layer. Master's thesis in Mathematical Sciences. Lund University, Sweden. 2001.

Yamashita T, Asaoka R, Tanaka M, et al. Relationship between position of peak retinal nerve fiber layer thickness and retinal arteries on sectoral retinal nerve fiber layer thickness. Invest Ophthalmol Vis Sci. 2013;54:5481-5488.